OPEN ACCESS



MHD Turbulent Power Anisotropy in the Inner Heliosphere

L. Adhikari ¹, G. P. Zank ¹, L.-L. Zhao ¹, and D. Telloni ²

Abstract

We study anisotropic magnetohydrodynamic (MHD) turbulence in the slow solar wind measured by Parker Solar Probe (PSP) and Solar Orbiter (SolO) during its first orbit from the perspective of variance anisotropy and correlation anisotropy. We use the Belcher & Davis approach (M1) and a new method (M2) that decomposes a fluctuating vector into parallel and perpendicular fluctuating vectors. M1 and M2 calculate the transverse and parallel turbulence components relative to the mean magnetic field direction. The parallel turbulence component is regarded as compressible turbulence, and the transverse turbulence component as incompressible turbulence, which can be either Alfvénic or 2D. The transverse turbulence energy is calculated from M1 and M2, and the transverse correlation length from M2. We obtain the 2D and slab turbulence energy and the corresponding correlation lengths from those transverse turbulence components that satisfy an angle between the mean solar wind flow speed and mean magnetic field $\theta_{\rm UB}$ of either (i) 65° < $\theta_{\rm UB}$ < 115° or (ii) 0° < $\theta_{\rm UB}$ < 25° (155° < $\theta_{\rm UB}$ < 180°), respectively. We find that the 2D turbulence component is not typically observed by PSP near perihelion, but the 2D component dominates turbulence in the inner heliosphere. We compare the detailed theoretical results of a nearly incompressible MHD turbulence transport model with the observed results of PSP and SolO measurements, finding good agreement between them.

Unified Astronomy Thesaurus concepts: Interplanetary turbulence (830); Slow solar wind (1873); Solar wind (1534)

1. Introduction

Anisotropy is one of the important properties of solar wind turbulence. Anisotropy has been studied via (i) the power spectral indices of the perpendicular k_{\perp} and parallel k_{\parallel} wavenumbers, i.e., spectral anisotropy (Horbury et al. 2008; Podesta 2009; Wicks et al. 2010; Narita et al. 2010; He et al. 2013; Bruno & Telloni 2015; Zhao et al. 2022); (ii) turbulent power in directions parallel and perpendicular to the mean magnetic field or variance anisotropy (Montgomery 1982; Matthaeus et al. 1990; Bieber et al. 1996; Milano et al. 2004; Smith et al. 2006; Osman & Horbury 2009a, 2009b; Ruiz et al. 2011; Weygand et al. 2011; Horbury et al. 2012; Weygand et al. 2013; Pine et al. 2020; Adhikari et al. 2021a; Zank et al. 2021; Zhao et al. 2022), and (iii) the correlation length in directions parallel and perpendicular to the mean magnetic field i.e., correlation anisotropy (Dasso et al. 2005; Matthaeus et al. 2005; Osman & Horbury 2007; Dasso et al. 2008; Weygand et al. 2009; Wang et al. 2019; Bandyopadhyay & McComas 2021). In the presence of a large-scale magnetic field, the variance anisotropy is determined by the relative magnitudes of the fluctuations in directions parallel and perpendicular to the mean magnetic field, and spectral anisotropy is determined with respect to the direction of k. These measures are therefore unique, and there is no dependence between them (Matthaeus et al. 1996; Oughton et al. 2015). Although they can be set separately (as an initial condition), it is possible that the dynamics may couple the two aspects.

Original content from this work may be used under the terms of the Creative Commons Attribution 4.0 licence. Any further distribution of this work must maintain attribution to the author(s) and the title of the work, journal citation and DOI.

Using a wavelet technique for high-speed streams in the ecliptic plane near solar minimum, Podesta (2009) studied the dependence of solar wind power spectra in the direction of the local mean magnetic field and found that the power-law exponent in the inertial range changes continuously from -1.6 ± 0.1 in the direction perpendicular to the mean magnetic field to -2 ± 0.1 in the direction parallel to the mean magnetic field. This is also consistent with Horbury et al. (2008), who found the magnetic power-law indices of -2 and -5/3 in flow directions parallel and perpendicular to the mean magnetic field. These observed results were interpreted as supporting the critical balance (CB) theory (Goldreich & Sridhar 1995), which requires $\sigma_c \sim 0$, where σ_c is the normalized cross helicity. Wang et al. (2014) found that in the presence of intermittency the spectral index for parallel magnetic fluctuations is -2, while the spectral power index is similar for k_{\perp} and $k_{||}$ in the absence of intermittency. Wang et al. (2015) reported that the spectral index for parallel magnetic fluctuations can be -2or -5/3 for moderate or small amplitude fluctuations. By perpendicular fluctuations, we mean that the fluctuating magnetic field components are transverse to the mean magnetic field **B**, i.e., $\mathbf{B} = B_0 \hat{z}$, δB_x , $\delta B_y \neq 0$, and $\delta B_z = 0$, and by parallel fluctuating magnetic field components, we mean that the $\delta B_z \neq 0$, $\delta B_x = \delta B_y = 0$.

In highly field-aligned flows, Telloni et al. (2019) and Zhao et al. (2020), using Wind and Parker Solar Probe (PSP) data sets, respectively, found a power-law index of -5/3. This is inconsistent with the predictions of CB theory, which requires that $\sigma_c \sim 0$, and it further introduces a puzzle about why the inertial range should possess a Kolmogorov-like spectrum in the apparent absence of counter-propagating Alfvén waves, needed to initiate the nonlinear interactions. A recently developed spectral theory based on the 2D + slab turbulence

¹ Center for Space Plasma and Aeronomic Research (CSPAR), and Department of Space Science, University of Alabama in Huntsville, Huntsville, AL 35899, USA la0004@uah.edu

National Institute for Astrophysics Astrophysical Observatory of Torino Via Osservatorio 20, I-10025 Pino Torinese, Italy Received 2022 March 1; revised 2022 May 16; accepted 2022 May 16; published 2022 July 4

superposition model (Zank et al. 2020) explains the formation of a spectral index -5/3 in highly field-aligned flows, as well as predicting, under certain conditions, that $E(k_{||}) \propto k_{||}^{-5/3}$ for arbitrary values of σ_c .

A review by Oughton et al. (2015) discusses the power anisotropy in solar wind turbulence from the inertial range to the dissipation scale. On using Advanced Composition Explorer (ACE) magnetometer data, Hamilton et al. (2008) found that the average wavevectors are more field aligned in the dissipation range than in the inertial range, and the fieldaligned wavevectors play a significant role in the formation of dissipation range. In the inner heliosphere from 0.3-1 au, MacBride et al. (2010) used Helios 1 magnetic field data sets to find that 80% of the turbulence energy resides in the wavevector perpendicular to the mean magnetic field (i.e., 2D advected fluctuations), consistent with the results of Bieber et al. (1996). They also found that the perpendicular and parallel wavevectors for the transverse small scales within the inertial range show similar energy distributions in the fast and slow solar wind flow (see also Hamilton et al. 2008). Belcher & Davis (1971) using Mariner magnetometer data calculated the ratio between the perpendicular and parallel variances of the magnetic field fluctuations, and found that the ratio is about 5 for a 3 hr long interval, and about 8 for a 22 minute long interval, indicating that the magnetic power anisotropy increases with decreasing length of the time interval, i.e., the decrease in the ratio of incompressible to compressible power implies either an increase in the power of the compressible fluctuations or a decrease in the power in incompressible fluctuations. They found that the magnetic power in each of the three orthogonal directions in a magnetic field-velocity coordinate system is of order 5:4:1. Bruno et al. (1999) investigated the effect of intermittency on the radial evolution of solar wind fluctuations anisotropy in the inner heliosphere at distances of 0.3, 0.7, and 0.9 au, and found that intermittency increases the anisotropy of both magnetic and velocity fluctuations. However, the magnetic anisotropy is larger in the presence of intermittency than the velocity anisotropy because magnetic fluctuations are thought to be more intermittent than velocity fluctuations. Bruno et al. (1999) defined anisotropy as the ratio between the total power perpendicular to the minimum variance direction and the power along the minimum variance direction. Horbury et al. (1995) investigated the anisotropy of inertial range turbulence in the polar heliosphere using Ulysses magnetometer data sets at distances of 1.7, 2.4, and 3.8 au. They found that the ratio of power transverse to the magnetic field to that parallel is about 30, and that the magnetic field fluctuations in directions parallel and perpendicular to the magnetic field become more isotropic with distance. Using Wind data sets, Leamon et al. (1998) found that the ratio between the total magnetic variances transverse to and aligned with the mean field is at a ratio of 10.4:1 at the high-frequency end of the inertial range. Similarly, Podesta (2009) using Stereo magnetometer data sets found that the power in directions perpendicular to the mean magnetic field in the inertial range is larger than the power in the parallel direction by factors ranging from approximately 2 near the middle of the inertial range to a factor of about 7 at the upper end of the inertial range. Using Voyager and ACE observations, Pine et al. (2020) studied the anisotropy of magnetic field fluctuations in the inertial range from 1-45 au from two perspectives: (i) the ratio of power associated with

fluctuations perpendicular and parallel to the mean magnetic field, and (ii) the ratio of power in two components perpendicular to the magnetic field. In the first case, anisotropy can be affected by the ratio of proton thermal energy and magnetic energy, and the magnetic compressibility. In the second case, the anisotropy may depend on the orientation of the mean field relative to the radial (solar wind velocity) direction, relating to the nature of the sampling and the spacecraft's ability to measure wavevectors parallel or perpendicular to the flow and magnetic field.

Dasso et al. (2005) studied the correlation anisotropy in the middle of the inertial range using 5 yr of ACE magnetometer data sets, in which the fast solar wind is more dominated by fluctuations with wavevectors k quasi-parallel to the local mean magnetic field, and the slow solar wind is more dominated by quasi-perpendicular fluctuations wavevectors. Figure 1 in Dasso et al. (2005) shows that the correlation length of the magnetic field fluctuations in the perpendicular direction is smaller than that in the parallel direction in the slow solar wind, and shows opposite characteristics in the fast solar wind. Wang et al. (2019) further analyzed the correlation anisotropy in the fast and slow solar wind for time intervals of lengths 2 days, 1 day, 10 hr, 2 hr, and 1 hr. In the 2 day long interval, their results are similar to Dasso et al. (2005). However, they also found that the correlation lengths in directions parallel and perpendicular to the mean magnetic field are approximately equal in the 1 hr long interval.

Several theoretical and numerical methods have been developed to study the power anisotropy of the turbulent solar wind (Montgomery & Turner 1981; Shebalin et al. 1983; Grappin 1986; Zank & Matthaeus 1992a, 1992b, 1993; Grappin et al. 1993; Goldreich & Sridhar 1995; Ghosh et al. 1998; Zank et al. 2020). One approach is to regard turbulence as a superposition of majority 2D turbulence and a minority slab turbulence, in which $\sim 80\%$ of the turbulent power is located in the direction perpendicular to the mean magnetic field, and $\sim 20\%$ of the turbulent power in the parallel direction (Zank & Matthaeus 1992a, 1992b, 1993). Such a dominant turbulent perpendicular energy from observations of the interplanetary magnetic field was also found at 1 au (Bieber et al. 1996). Recently, Bandyopadhyay & McComas (2021) and Zhao et al. (2022) used PSP magnetometer data sets and the Bieber test (Bieber et al. 1996) to find that the relative power in 2D magnetic field fluctuations is smaller closer to the Sun than far from the Sun. Zhao et al. (2022) found that over the distance 0.13-0.3 au, the ratio between the amplitudes of the 2D and slab turbulence is about 0.43 (or 30%:70%), whereas from 0.3–0.6 au, the ratio between the amplitudes of the 2D and slab turbulence is about 1.63 (or 62%:38%). The Bieber test assumes that all spectra satisfy $k^{-5/3}$, which is not necessarily true for slab as we have seen, and one needs to use a more general formulation for an arbitrary slab spectrum (Zank et al. 2020). In this manuscript, we calculate the 2D and slab energies in transverse magnetic field fluctuations through the covariance analysis using the approach of Belcher & Davis (1971) and a new method. We also calculate the 2D and slab correlation lengths of the magnetic field fluctuations. In addition, we calculate the 2D and slab Elsässer energies, fluctuating kinetic and magnetic energies, normalized residual energy, normalized cross helicity, and the corresponding 2D and slab correlation lengths. Finally, we compare the observed results with the theoretical results of the NI MHD turbulence

Table 1
2D and Slab Turbulence Quantities

Turbulent Quantities				
2D and slab outward/inward Elsässer energies				
Fluctuating magnetic energy				
Fluctuating kinetic energy				
Normalized residual energy				
Normalized cross helicity				
Correlation length corresponding to Elsässer energies				
Correlation length corresponding to residual energy				
Correlation length of magnetic field fluctuations				
Correlation length of velocity fluctuations				

Note. The superscripts " ∞ " and "*" denote the theoretical 2D and NI/slab quantities, respectively. The subscripts "2D" and "sl" denote the observed 2D and slab quantities, respectively. The "+" and "-" signs denote the outward and inward directions relative to the Sun

model (Zank et al. 2017) as a function of heliocentric distance. We summarize the theoretical and observed 2D and slab turbulence quantities in Table 1.

A theoretical NI MHD turbulence transport model for small (\ll 1) and O(1) plasma beta regimes (Zank et al. 2017) can be used to calculate the turbulent power anisotropy in the energycontaining range. The energy-containing range turbulence transport models assume a Kolmogorov or IK phenomenology to describe the cascade of turbulence energy through the inertial range and its eventual dissipation. Here, the former is a strong turbulence (for which nonlinear effects are dominant) approach, whereas IK is inherently a weak turbulence approach (i.e., essentially nonlinear corrections to Alfvén waves). Adhikari et al. (2017b) developed a theoretical model for the turbulent power anisotropy of the magnetic field fluctuations in the inertial range. They found that the power anisotropy in magnetic field fluctuating energy in the inertial range increases slightly from ~ 1.2 to $\sim 4-5$ au, and then decreases with increasing distance. Therefore, in this model, power anisotropy in magnetic turbulence near 1 au evolves toward a state of increasingly isotropic magnetic turbulence power in the outer heliosphere. In part, this is due to the presence of turbulent shear and pickup ions creation that act as sources of turbulence. In a similar study, Adhikari et al. (2018) showed that in the absence of interplanetary sources of turbulence, the power anisotropy in magnetic field fluctuations in the energycontaining range and the inertial range is larger during the 2009 solar minimum than that during the 2003 and 2015 solar maxima over the distance 1-75 au. The power anisotropy in magnetic field fluctuations may depend on the solar wind speed (Oughton et al. 2015). The speed during the 2009 solar minimum was 359.48 kms⁻¹, and during the 2003 and 2015 solar maxima it was 493.31 and 412.25 kms⁻¹, respectively (Zhao et al. 2018). Since the solar wind speed in the prior case is smaller than that in the latter case, turbulence was more anisotropic during the 2009 solar minimum than during the 2003 and 2015 solar maxima.

The outline of the manuscript is as follows. Section 2 introduces the solar wind model. Section 3 discusses the NI MHD turbulence quantities, and the Appendix presents the NI MHD turbulence transport model equations. Section 4 discusses the data analysis methodology. Sections 5 and 6 compare the theoretical and observed results. Finally, Section 7 provides a discussion and conclusions.

2. Solar Wind Model

The 1D spherically symmetric steady-state continuity, momentum, and proton and electron pressure equations describe the radial evolution of the solar wind mass density ρ , speed U, and thermal proton pressure P_p and electron pressure P_e , respectively, and are given by

$$\frac{d}{dr}(r^2\rho U) = 0,\tag{1}$$

$$\rho U \frac{dU}{dr} = -\frac{dP_p}{dr} - \frac{dP_e}{dr},\tag{2}$$

$$U\frac{dP_p}{dr} + \gamma P_p \frac{dU}{dr} + 2\gamma \frac{U}{r} P_p = (\gamma - 1)(\nu_{pe}(P_e - P_p) + f_p S_t),$$
(3)

$$U\frac{dP_e}{dr} + \gamma P_e \frac{dU}{dr} + 2\gamma \frac{U}{r} P_e = (\gamma - 1)$$

$$\times [\nu_{ep}(P_p - P_e) - \nabla \cdot \mathbf{q}_e + (1 - f_p) S_t], \tag{4}$$

where ν_{pe} and ν_{ep} are the rates of proton-electron Coulomb collisions (Barakat & Schunk 1982; Zank 2014), r is the heliocentric distance, and S_t is a turbulence heating term. Here, we neglect the gravitational force and the magnetic force $(\mathbf{J} \times \mathbf{B})_r = -1/(\mu_0 r) B_{\phi} d/dr (r B_{\phi})$ in Equation (2). We only include the thermal proton and electron forces, which drive the solar wind in the inner heliosphere. The parameter f_p denotes the fraction of turbulence energy that heats the solar wind protons, $(1 - f_p)$ the fraction of turbulence energy that heats the solar wind electrons, and $\gamma (=5/3)$ is the polytropic index. Equation (3) shows that turbulence energy, through S_t , and Coulomb collisions between solar wind protons and electrons influences the radial profile of the solar wind proton temperature. In addition to turbulence energy and Coulomb collisions between solar wind protons and electrons, the electron heat flux q_e also influences the radial profile of the solar wind electron temperature (Cranmer et al. 2009; Breech et al. 2009; Engelbrecht & Strauss 2018; Chhiber et al. 2019; Adhikari et al. 2021a, 2021b; Zank et al. 2021). Here, we assume that the electron density n_e and the proton density n_p are approximately equal. The rate of proton-electron Coulomb collisions is given by Cranmer et al. (2009) as

$$\nu_{pe} \approx 8.4 \times 10^{-9} \left(\frac{n_e}{2.5 \text{ cm}^{-3}} \right) \left(\frac{T_e}{10^5 \text{ K}} \right)^{-3/2} \text{ s}^{-1},$$
 (5)

where the Coulomb collisional frequencies are assumed to be equal for protons and electrons, i.e., $n_e \nu_{ep} \sim n_p \nu_{pe}$. The electron heat flux is given by the empirical formula (Cranmer et al. 2009),

$$\ln\left(\frac{q_{\parallel,e}}{q_0}\right) = -0.7037 - 2.115x - 0.2545x^2,\tag{6}$$

which is obtained by fitting the observed electron heat flux from Helios 2 over the distance 0.3–1 au (Pilipp et al. 1990). Here, $x \equiv \ln(r/\text{au})$ and $q_0 = 0.01 \text{ erg cm}^{-2} \text{ s}^{-1}$. The term $\nabla \cdot \mathbf{q}_e$ is expressed as (Cranmer et al. 2009),

$$\nabla \cdot \boldsymbol{q}_e = \frac{1}{r^2} \frac{\partial}{\partial r} (r^2 q_{\parallel} \cos^2 \phi), \tag{7}$$

where ϕ is the Parker spiral angle,

$$\tan \phi = \frac{\Omega r \sin \theta}{U},$$

and $\Omega = 2.7 \times 10^{-6} \text{ rad s}^{-1}$ is the solar rotation frequency. We choose a colatitude $\theta = 90^{\circ}$ to compare the theoretical results with the PSP and Solar Orbiter (SolO) measurements.

The turbulent heating term S_t can be expressed as

$$S_{t} = \alpha m_{p} n_{s} \left[\frac{\langle z^{\infty+2} \rangle \langle z^{\infty-2} \rangle^{1/2}}{\lambda_{\infty}^{+}} + \frac{\langle z^{\infty-2} \rangle \langle z^{\infty+2} \rangle^{1/2}}{\lambda_{\infty}^{+}} + \frac{\langle z^{\infty+2} \rangle \langle z^{\infty-2} \rangle^{1/2}}{\lambda_{\infty}^{+}} + \frac{\langle z^{\infty-2} \rangle \langle z^{\infty+2} \rangle^{1/2}}{\lambda_{\infty}^{-}} \right],$$
(8)

where m_p is the proton mass, n_s is the solar wind proton density, and α is a von Kármán–Taylor constant. The terms inside the squared bracket [...] correspond to the dissipation of 2D turbulence and NI/slab (hereafter called the slab) turbulence. The various terms appearing in Equation (8) are discussed below.

3. NI MHD Turbulence Quantities

In the NI MHD notational convention, the magnetic field fluctuations B', the velocity fluctuations u', and the density fluctuations ρ' can be expressed as $B' = B^{\infty} + B^*$, $u' = u^{\infty} + u^*$, and $\rho' = \rho^{\infty} + \rho^*$ (Zank & Matthaeus 1992b, 1993), in which the leading order 2D fluctuations, and the minority slab fluctuations follow the ordering M_A^t : $M_A^{t\,2}$ (Zank et al. 2017, 2020), where $M_A^t (\equiv \langle u^2 \rangle^{1/2} / V_{A0})$ is the turbulent Alfvén Mach number, $\langle u^2 \rangle^{1/2}$ the square root of the characteristic velocity fluctuations, and V_{A0} the large-scale Alfvén velocity. NI MHD theory is developed based on M_A^t being a small quantity. NI MHD in the plasma beta regimes of order 1 (i.e., $\beta_p \sim 1$) or much less than 1 (i.e., $\beta_p \ll 1$) predicts that solar wind turbulence is a superposition of the majority 2D turbulence component and a minority slab turbulence component (Zank & Matthaeus 1992b, 1993; Zank et al. 2017). The majority 2D and the minority slab Elsässer variables are given by Zank et al. (2017)

$$z^{\infty\pm} = u^{\infty} \pm \frac{B^{\infty}}{\sqrt{\mu_0 \rho_m}}, \quad z^{*\pm} = u^* \pm \frac{B^*}{\sqrt{\mu_0 \rho_m}},$$

where ρ_m is the mean solar wind mass density, and μ_0 the magnetic permeability. The 2D variances of the Elsässer variables $\langle z^{\pm 2} \rangle$, and the residual energy E_D , with analogous

definitions for the "*" superscript quantities,

$$\begin{split} \langle z^{\infty\pm2} \rangle &= \langle z^{\infty\pm} \cdot z^{\infty\pm} \rangle \text{ and } E_D^\infty \\ &\equiv \langle z^{\infty+} \cdot z^{\infty-} \rangle = \langle u^{\infty2} \rangle - \langle B^{\infty2} / \mu_0 \rho_m \rangle. \end{split}$$

The Elsässer energies and the residual energy weighted length scales allow us to introduce the correlation lengths using

$$\begin{split} L_{\infty}^{\pm} &= \int \langle z^{\infty \pm} \cdot z^{\infty \pm \prime} \rangle dy \equiv \langle z^{\infty \pm 2} \rangle \lambda_{\infty}^{\pm}; \\ L_{D}^{\infty} &= \int \langle z^{\infty +} \cdot z^{\infty - \prime} + z^{\infty + \prime} \cdot z^{\infty -} \rangle dy \equiv E_{D}^{\infty} \lambda_{D}^{\infty}, \end{split}$$

where y = |y| is the spatial lag between fluctuations, $z^{\infty,*-\prime}$ the lagged Elsässer variables, and λ^{\pm} and λ_D are the correlation lengths corresponding to the outward and inward Elsässer energies, and the residual energy.

Similarly, other 2D turbulence quantities, with corresponding definitions for the "*" superscript quantities (Zank et al. 2012; Dosch et al. 2013),

$$E_{T}^{\infty} \equiv \frac{\langle z^{\infty+2} \rangle + \langle z^{\infty-2} \rangle}{2} = \langle u^{\infty2} \rangle + \langle B^{\infty2} / \mu_{0} \rho_{m} \rangle$$

$$E_{C}^{\infty} \equiv \frac{\langle z^{\infty+2} \rangle - \langle z^{\infty-2} \rangle}{2} = 2 \langle u^{\infty} \cdot B^{\infty} / \sqrt{\mu_{0} \rho_{m}} \rangle,$$

$$r_{A}^{\infty} = \frac{\langle u^{\infty2} \rangle}{E_{b}^{\infty}} = \frac{E_{T}^{\infty} + E_{D}^{\infty}}{E_{T}^{\infty} - E_{D}^{\infty}} = \frac{1 + \sigma_{D}^{\infty}}{1 - \sigma_{D}^{\infty}},$$

$$\langle u^{\infty2} \rangle = \frac{E_{T}^{\infty} + E_{D}^{\infty}}{2}, \quad E_{b}^{\infty} = \left\langle \frac{B^{\infty2}}{\mu_{0} \rho_{m}} \right\rangle = \frac{E_{T}^{\infty} - E_{D}^{\infty}}{2},$$

$$\sigma_{D}^{\infty} = \frac{E_{D}^{\infty}}{E_{T}^{\infty}}, \quad \sigma_{c}^{\infty} = \frac{E_{C}^{\infty}}{E_{T}^{\infty}},$$

$$\lambda_{u}^{\infty} \equiv \frac{\langle z^{\infty+2} \rangle \lambda_{w}^{+} + \langle z^{\infty-2} \rangle \lambda_{w}^{-} + E_{D}^{\infty} \lambda_{D}^{\infty}}{4 \langle u^{\infty2} \rangle},$$

$$\lambda_{B}^{\infty} \equiv \frac{\langle z^{\infty+2} \rangle \lambda_{w}^{+} + \langle z^{\infty-2} \rangle \lambda_{w}^{-} - E_{D}^{\infty} \lambda_{D}^{\infty}}{4 \langle u^{\infty2} \rangle},$$
(9)

where E_T^{∞} is the total turbulent energy, E_C^{∞} the cross helicity, E_b^{∞} the fluctuating magnetic energy density, and r_A^{∞} the Alfvén ratio. Note that the Elsässer-based versus u/b-based definitions contain identical information and it is a matter of convenience and situation in deciding which to use.

4. Data Analysis

We select the first orbit PSP Solar Wind Electrons Alphas & Protons (SWEAP; Kasper et al. 2016) and FIELDs (Bale et al. 2016) data sets, and SolO magnetometer (Horbury et al. 2020) and Solar Wind Analyzer-Proton and Alpha Sensor plasma (Owen et al. 2020) data sets corresponding to the slow solar wind to calculate the 2D and slab turbulence energies and the corresponding 2D and slab correlation lengths. We use two methods: (i) the approach of Belcher & Davis (1971)—Method 1 (or M1), and (ii) a new method—Method 2 (or M2). These two methods yield the turbulence components in directions parallel and transverse to the mean magnetic field. The prior is regarded as compressible turbulence, and the latter as incompressible turbulence, which can be either Alfvénic or 2D. We first calculate the various transverse turbulence energies using M1 and M2, and the corresponding transverse correlation lengths using M2. M1 directly calculates the transverse turbulence energy. By contrast, M2 first calculates the R, T, and N components of the fluctuating perpendicular solar wind speed and the magnetic field, and then calculates the transverse turbulence energy and the transverse correlation

length. An important difference between the methods is that M2 calculates the correlation matrix for the fluctuations, while M1 calculates only the variance matrix (=correlation matrix evaluated at zero lag). We then determine the various slab turbulence energies and the corresponding correlation lengths (see Table 1) by selecting those transverse turbulence components that satisfy the range of angles between the mean flow and mean magnetic field θ_{UB} values according to $0^{\circ} < \theta_{\rm UB} < 25^{\circ} \ (155^{\circ} < \theta_{\rm UB} < 180^{\circ})$. In this case, the geometry between the mean flow and magnetic field is parallel (or radial). Similarly, we determine the various 2D turbulence energies and correlation lengths by selecting those transverse turbulence components that satisfy θ_{UB} values between $65^{\circ} < \theta_{\rm UB} < 115^{\circ}$. In this case, the geometry between the mean flow and magnetic field is perpendicular. We compare the results of the new method (M2), with the results obtained from the Belcher & Davis (1971) approach (M1), and the NI MHD turbulence model (Zank et al. 2017).

4.1. Method 1

Belcher & Davis (1971) introduced the following expression for the parallel variance of the magnetic field fluctuations $P_{||}$:

$$P_{\parallel} = \frac{\sum \langle B_i \rangle S_{ij} \langle B_j \rangle}{|\langle \mathbf{B} \rangle|^2},\tag{10}$$

and the transverse variance of the magnetic field fluctuations P_{\perp} is given by

$$P_{\perp} = P_{s} - P_{\parallel},\tag{11}$$

where

$$S_{ii} = \langle b_i b_i \rangle - \langle b_i \rangle \langle b_i \rangle$$

is a 3×3 matrix, formed by the R, T, and N components of the fluctuating magnetic field b, and P_s denotes the trace of a variance matrix S_{ij} . Using Equations (10) and (11) we calculate the transverse magnetic field fluctuations in a plane perpendicular to the mean magnetic field. To calculate the transverse Elsässer energies and fluctuating kinetic energy, the variance matrix S_{ij} is formed by the R, T, and N components of the Elsässer variables and the fluctuating solar wind speed, respectively (Adhikari et al. 2021c). Then, we calculate the observed 2D and slab turbulence energies based on two criteria discussed above.

4.2. Method 2

The alternative approach to calculate the various transverse and parallel Elsässer moments including various transverse and parallel correlation lengths is presented. A fluctuating vector $\mathbf{a}(=a_r\hat{r}+a_t\hat{t}+a_n\hat{n})$, where a_r , a_t , and a_n are the R, T, and N components of a vector \mathbf{a}) can be written in terms of parallel and perpendicular vectors as

$$\boldsymbol{a} = \boldsymbol{a}_{||} + \boldsymbol{a}_{\perp} = a_{||}\hat{b} + \boldsymbol{a}_{\perp},$$

where $\hat{b} = B/|B|$ is the unit vector, |B| is the magnitude of the mean magnetic field B, and a_{\perp} and $a_{||}(=a_{||}\hat{b})$ are the perpendicular and parallel vectors, respectively. The parallel component $a_{||}$ can be written as

$$a_{\rm II} = \boldsymbol{a} \cdot \hat{\boldsymbol{b}},\tag{12}$$

and the perpendicular vector \mathbf{a}_{\perp} ,

$$\mathbf{a}_{\perp} = -\hat{b} \times (\hat{b} \times \mathbf{a}) = \frac{(\mathbf{B} \times \mathbf{a}) \times \mathbf{B}}{|\mathbf{B}|^2},$$
 (13)

where $|\boldsymbol{B}|^2 = B_R^2 + B_T^2 + B_N^2$ is the square of the magnitude of the mean magnetic field, and B_R , B_T , and B_N are the R, T, and N components of the mean magnetic field. The perpendicular vector \boldsymbol{a}_{\perp} can be written in terms of R, T, and N components as

$$\mathbf{a}_{\perp} = \frac{C_T B_N - C_N B_T}{|\mathbf{B}|^2} \hat{r} + \frac{C_N B_R - C_R B_N}{|\mathbf{B}|^2} \hat{t} + \frac{C_R B_T - C_T B_R}{|\mathbf{B}|^2} \hat{n},$$
(14)

where $C_R = B_T a_n - B_N a_t$, $C_T = B_N a_r - B_R a_n$, and $C_N = B_R a_t - B_T a_r$. Similarly, the parallel vector $\mathbf{a}_{||}$ is given by

$$\mathbf{a}_{\parallel} = \frac{a_{r}B_{R} + a_{t}B_{T} + a_{n}B_{N}}{B_{R}^{2} + B_{T}^{2} + B_{N}^{2}} B_{R}\hat{r} + \frac{a_{r}B_{R} + a_{t}B_{T} + a_{n}B_{N}}{B_{R}^{2} + B_{T}^{2} + B_{N}^{2}} B_{T} + \frac{a_{r}B_{R} + a_{t}B_{T} + a_{n}B_{N}}{B_{R}^{2} + B_{T}^{2} + B_{N}^{2}} B_{N}\hat{n}.$$

$$(15)$$

The first, second, and third terms on the right-hand side (rhs) of Equations (14) and (15) yield the R, T, and N components of the perpendicular and parallel fluctuating magnetic field and solar wind speed. Using the R, T, and N components of the perpendicular fluctuating fields, we calculate the transverse turbulence energy and correlation length by following the same approach as in our previous papers (Zank et al. 1996; Adhikari et al. 2014, 2015, 2017a; Shiota et al. 2017; Zhao et al. 2018; Adhikari et al. 2021c). We then calculate the observed 2D and slab turbulence components from the transverse values using the criteria based on $\theta_{\rm UB}$ values.

5. Radial Evolution of 2D and Slab Turbulence

We use a Runge-Kutta fourth-order method to solve the coupled solar wind and NI MHD 2D and slab turbulence transport equations from the perihelion of the first orbit of PSP $(\sim 36.66 R_{\odot})$ to 177 R_{\odot} . To solve the coupled solar wind and NI MHD turbulence transport equations, we use the boundary conditions shown in Table 2. Table 3 shows the parameter values used in the NI MHD turbulence transport model equations. The boundary conditions and the parameter values are chosen in such a way that the radial profile of the theoretical result is close to the observed result. We compare the theoretical results of the 2D and slab turbulence energy and correlation length, and the solar wind parameters with PSP and SolO measurements as a function of heliocentric distance. For the slow solar wind of PSP, we use the data sets at times (DOY:HR: MIN): 309:3:18-311:12:44, 313:9:29-314:3:20, 315:16:52 -317:22:59, 324:22:51-325:13:19, and 332:7:52-333:23:57 of the year 2018 (see Adhikari et al. 2020a). Similarly, for the slow solar wind of SolO, we use the data sets at times (YY:MN: DD): 2020-07-17, 2020-07-18, 2020-07-22, 2020-07-30, 2020-08-02, 2020-08-03, 2020-08-04, 2020-08-05, 2020-08-07, 2020-08-08, 2020-08-09, 2020-08-11, and 2020-08-13 (see Adhikari et al. 2021c). During the period of our study, PSP and SolO stay within a latitude of 5°. Although PSP and SolO do not observe the same plasma parcel, they measure similar types of slow solar wind. Here, PSP data intervals vary from about 1 day to 2 days, while SolO data intervals are 1 day long. In every \sim 1–2 day long

Parameters	Values	Parameters	Values
$\langle z^{\infty+2} \rangle \text{ (km}^2 \text{ s}^{-2})$	12,000	$\langle z^{*+2} \rangle \text{ (km}^2 \text{ s}^{-2})$	6000
$\langle z^{\infty-2} \rangle \text{ (km}^2 \text{ s}^{-2})$	600	$\langle z^{*-2} \rangle \text{ (km}^2 \text{ s}^{-2})$	300
$E_D^{\infty} (\mathrm{km}^2 \mathrm{s}^{-2})$	-300	$E_D^* (\mathrm{km}^2 \mathrm{s}^{-2})$	-200
λ_{∞}^{+} (km)	8.4×10^{4}	λ_*^+ (km)	1.2×10^{5}
λ_{∞}^{-} (km)	1.05×10^{5}	λ_*^- (km)	1.5×10^{5}
λ_D^{∞} (km)	1.38×10^{6}	λ_D^* (km)	1.53×10^{6}
$T_p(\mathbf{K})$	2.0×10^{5}	T_e (K)	1.6×10^{5}
$U (\mathrm{km \ s}^{-1})$	350	$\langle \rho^{\infty 2} \rangle \text{ (cm}^{-6})$	1.16×10^{3}
$\rho (\mathrm{cm}^{-3})$	207.16		

Note. The electron density is assumed approximately equal to the proton density, $n_e \approx n_p$. The proton and electron thermal pressure is determined from $P_p = n_p k_B T_p$ and $P_e = n_e k_B T_e$, respectively

Table 3
Values of The Parameters Used for the Turbulence Model

Parameters	Values
$\overline{V_{A0}}$	$102.73 \text{ (km s}^{-1}\text{)}$
α	0.02
β	0.01
b	0.28
$C_{ m sh}^+$	0.1
$C_{ m sh}^-$	0.1
$C_{ m sh}^{E_D}$	0.1
$C_{ m sh}^{*+}$	0.1
$C_{ m sh}^{*-}$	0.1
$eta \ b \ C_{ m sh}^+ \ C_{ m sh}^- \ C_{ m sh}^{E_D} \ C_{ m sh}^{*+} \ C_{ m sh}^{*-} $	-0.01
η	0.01
$\stackrel{\cdot}{\Delta} U$	$200 \text{ (km s}^{-1})$

data set from PSP, and day long data set from SolO, we first calculate the transverse turbulence energy using M1 and M2, and the correlation length using M2 in 4 hr long moving intervals. We then determine the 2D and slab turbulence energy and the corresponding 2D and slab correlation lengths. The 2D components are determined from the transverse components in the \sim 1–2 day period that satisfy the criterion 65° < $\theta_{\rm UB}$ < 115°, and taking averaged values. Similarly, the slab turbulence components are determined from those transverse components in the \sim 1–2 day period that satisfy the values 0° < $\theta_{\rm UB}$ < 25° (155° < $\theta_{\rm UB}$ < 180°), and taking averaged values. In doing so, we assume that the solar wind plasma properties are similar within the \sim 1–2 day period. In the case of SolO, we further bin the observed results using a 7 R_{\odot} bin width.

As discussed above, our method for distinguishing between 2D and slab turbulence uses the geometry between the background fields. Only propagating Alfvénic fluctuations with wavevectors parallel to a mean magnetic field can be observed when the mean magnetic field is parallel to the radial solar wind flow vector. The approach is analogous to that of Telloni et al. (2019) and Zhao et al. (2020), who identified unidirectionally propagating Alfvén waves in a highly aligned magnetic field—solar wind flows. Similarly, Zank et al. (2022) argued that PSP observes only the slab turbulence component in the sub- and super-Alfvénic regions during encounter 8 near perihelion based on $\theta_{\rm UB}$ values of 15° and 18°, respectively. This method is closely related to the Bieber et al. (1996)

approach in distinguishing between 2D turbulence and slab turbulence near 1 au. According to Equation (81) of Bieber et al. (1996) (see also Zank et al. 2020), as the field angle increases, the slab contribution decreases while the 2D contribution increases, and vice versa. In this manuscript, we assume that when the background fields are parallel, only the slab contribution can be measured (*is visible*), and when the background fields are perpendicular, only the 2D contribution is visible. The angle between the measurement direction and mean field direction restricts what can be obtained from the measurements but, it should be emphasized, this does not reflect the possible range of fluctuations that are likely present in the flow, i.e., observing Alfvénic fluctuations in a highly magnetic field-aligned flow does not exclude the presence of advected 2D fluctuations, and vice versa.

Figure 1 shows a comparison between the theoretical and observed 2D and slab outward and inward Elsässer energies (A and B), fluctuating magnetic and kinetic energies (C and D). normalized residual energy (E), normalized cross helicity (F) and the variance of the density fluctuations (G) as a function of heliocentric distance. In the figure, the red curve identifies the theoretical majority 2D component, and the blue curve is the theoretical minority slab component. The red stars, cyan and brown stars with error bars, and green diamonds denote the observed 2D component. The blue stars, black and yellow stars with error bars, and magenta diamonds denote the observed slab component. The error denotes the standard error σ/\sqrt{n} , where n is the number of data points. Here, the red and blue stars (calculated by M2), and the green and magenta diamonds (calculated by M1) correspond to the results from the PSP data sets. Similarly, the cyan, and black stars with error bars (calculated by M2), and brown and yellow stars with error bars (calculated by M1) correspond to the results from SolO data sets. Over a distance \sim 36.7–129 R_{\odot} , PSP observes mostly the slab component (at distances \sim 36.66, \sim 48.85, \sim 60.29, and $\sim 100.72~R_{\odot}$) compared to the 2D component (at distances \sim 64.46 and \sim 129 R_{\odot}). Recall that the 2D and slab turbulence components are distinguished by using measurements made only in specific θ_{UB} ranges: (i) $65^{\circ} < \theta_{UB} < 115^{\circ}$, and (ii) $0^{\circ} < \theta_{UB} < 25^{\circ}$ ($155^{\circ} < \theta_{UB} < 180^{\circ}$), respectively. In case (i), the slab component is invisible to PSP (and SolO), and in case (ii), the 2D component is invisible to PSP (and SolO). For other angles θ_{UB} , PSP (and SolO) can observe both the 2D and slab components, allowing one to decompose the turbulence components into 2D and slab components. This is beyond the scope of this manuscript. Over a distance $\sim 142-176 R_{\odot}$, SolO observes the slab turbulence component at distances \sim 144, \sim 147.8, \sim 156.7, and \sim 167 R_{\odot} , and the 2D turbulence component at distances \sim 145, \sim 149.8, \sim 159.4, and \sim 168.5 R_{\odot} . We also note that the observed results in this manuscript are calculated over 4 hr long intervals in order to compare with theoretical results.

PSP observes primarily slab outward Elsässer energy $\langle z_{sl}^{+2} \rangle$ rather than 2D outward Elsässer energy $\langle z_{2D}^{+2} \rangle$ during its first encounter. In contrast, SolO observes both 2D and slab outward Elsässer energies frequently, with the 2D component being larger than the slab component. The theoretical $\langle z^{*+2} \rangle$ is consistent with that measured by PSP and SolO. However, the theoretical $\langle z^{*+2} \rangle$ is larger than that observed by PSP, but is consistent with that measured by SolO.

Similarly, PSP measures $\langle z_{sl}^{-2} \rangle$ near perihelion, and not $\langle z_{2D}^{-2} \rangle$, whereas SolO observes both slab and 2D components regularly.

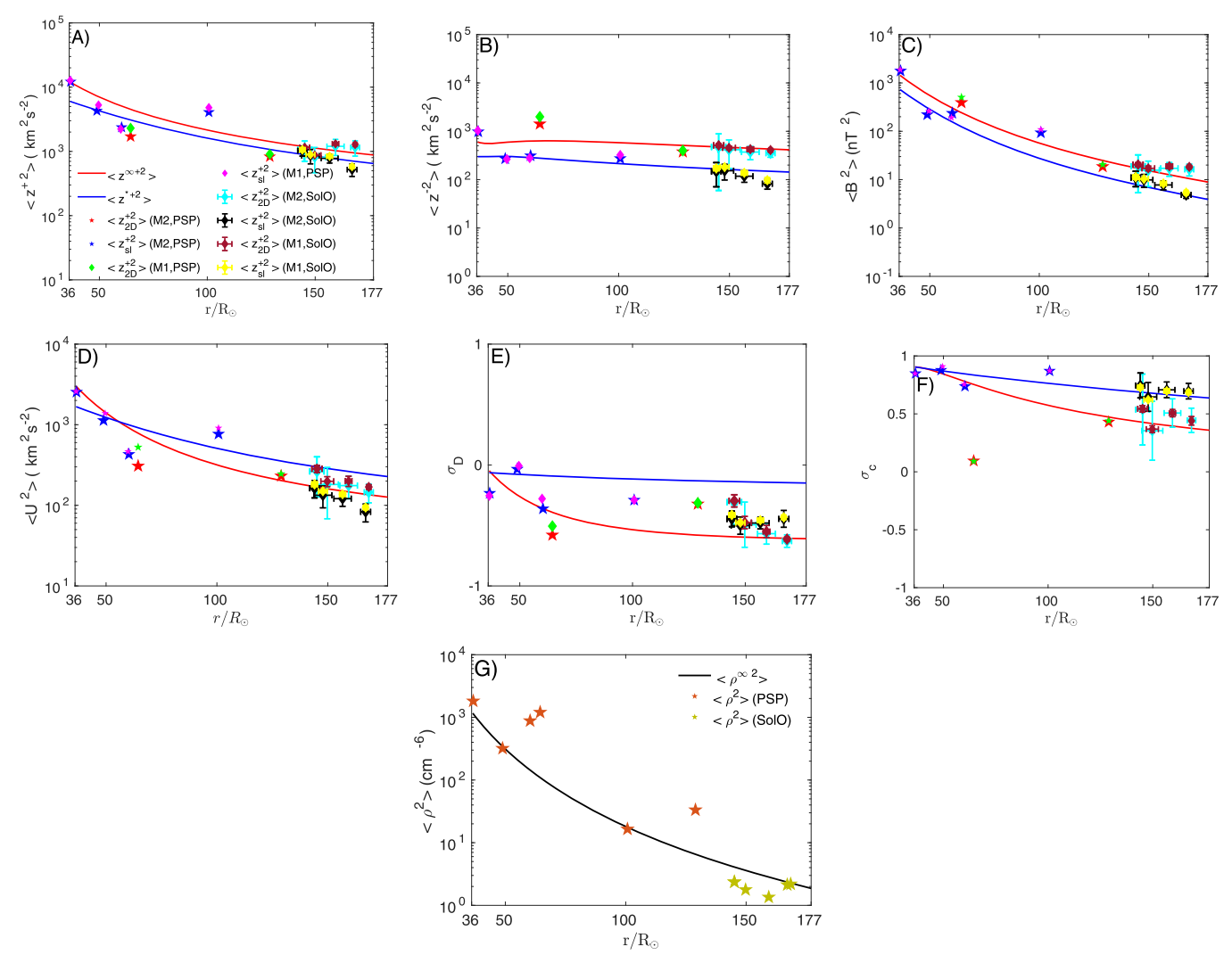


Figure 1. Comparison between the theoretical and observed 2D and slab Elsässer energies $\langle z^{\pm}2 \rangle$ (A and B), fluctuating magnetic energy (C), fluctuating kinetic energy (D), normalized residual energy (E), normalized cross helicity (F), and the variance of the density fluctuations (G) as a function of heliocentric distance. The solid red curve denotes the 2D component, and the solid blue curve the slab component. The red stars, cyan and brown stars with error bars, and green diamonds denote the observed 2D component. The blue stars, black and yellow stars with error bars, and magenta diamonds denote the observed slab component. The solid black curve in the bottom right panel denotes the theoretical variance of density fluctuations. The orange and light green stars denote the observed variance of density fluctuations.

The SolO observed $\langle z_{2D}^{-2} \rangle$ is larger than the SolO observed $\langle z_{sl}^{-2} \rangle$. The theoretical $\langle z^{\infty-2} \rangle$ increases slightly, and then decreases slowly with increasing heliocentric distance, and is consistent with the observed $\langle z_{2D}^{-2} \rangle$. The increase in $\langle z^{\infty-2} \rangle$ may be due to both the presence of a turbulent shear source, and gradients in the solar wind density, magnetic field, and solar wind speed (Coleman 1968; Zhou & Matthaeus 1990; Marsch & Tu 1993; Matthaeus et al. 1999; Breech et al. 2008; Adhikari et al. 2015). The theoretical $\langle z^*-2 \rangle$ decreases with increasing distance, and is similar to that observed by PSP and SolO.

Although the 2D turbulent magnetic energy component cannot be observed near the perihelion, the theoretical results and the observed results beyond $\sim\!64.46~R_{\odot}$ show that the 2D component is larger than the slab component, consistent with the NI MHD theory (Zank & Matthaeus 1992b, 1993) and observations (Bieber et al. 1996). Recently, Bandyopadhyay & McComas (2021) and Zhao et al. (2022) found that the relative power in 2D magnetic field fluctuations appears to be smaller closer to the Sun after analyzing PSP magnetometer data sets and applying the Bieber test (Bieber et al. 1996). However, these conclusions rely on several important assumptions, and

especially the assumption that the observed turbulence power density spectra in the inertial range correspond to Kolmogorov -5/3 power laws. In principle, the Bieber et al. (1996) test results can change if the power-law PSDs are different from the Kolmogorov form (Zank et al. 2020), particularly if the 2D and slab spectra differ as found by Zank et al. (2022), for example. Note that the Bieber et al. (1996) method assumes the same power law forms $k^{-5/3}$ for both 2D and slab turbulence. In Figure 1(C), the theoretical $\langle B^{\infty 2} \rangle$ and $\langle B^*2 \rangle$ are consistent with the corresponding observed turbulent magnetic energies. Similarly, PSP observes $\langle u_{sl}^2 \rangle$ near perihelion, whereas the observed $\langle u_{2D}^2 \rangle$ is larger than the observed $\langle u_{sl}^2 \rangle$ from 142–176 R_{\odot} . The theoretical $\langle u^{\infty 2} \rangle$ shows reasonable agreement with $\langle u_{2D}^2 \rangle$, whereas the theoretical $\langle u^*2 \rangle$ is in reasonable accord with PSP measurements, but is larger than SolO measurements.

Near the perihelion, the observed slab turbulence is less magnetically dominated (since the observed slab residual energy σ_{sl}^D is close to 0), and becomes more magnetically dominated with increasing distance. Compared to slab turbulence, 2D turbulence

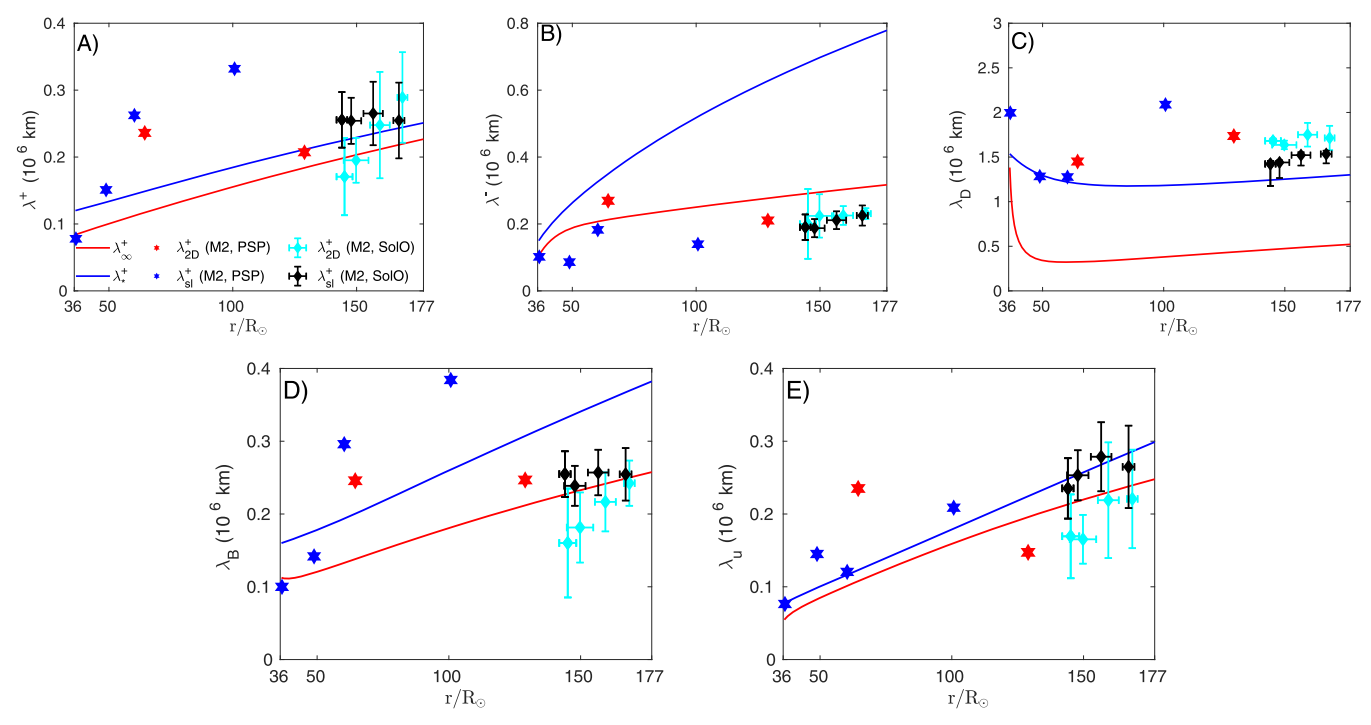


Figure 2. Comparison between the theoretical and observed 2D and slab correlation lengths corresponding to the energy in forward (A) and backward (B) propagating modes, the residual energy (C), the fluctuating magnetic energy (D), and the fluctuating kinetic energy (E) as a function of heliocentric distance. The solid red and blue curves denote the theoretical correlation length corresponding to 2D and slab components, respectively. The red stars and cyan diamonds with error bars represent the observed 2D correlation lengths. The blue stars and black diamonds with error bars represent the observed slab correlation lengths

is observed to be more dominated by the turbulent magnetic energy. SolO measurements show that the observed σ_{sl}^D decreases more slowly than the observed $\sigma_{2\mathrm{D}}^D$. The theoretical σ_{D}^* is larger than the observed σ_{sl}^D , and decreases as distance increases. The theoretical σ_{D}^{∞} decreases more rapidly initially, then more gradually as distance increases, and is close to observations. The theoretical slab cross helicity σ_{c}^* is similar to the theoretical 2D cross helicity σ_{c}^{∞} near the perihelion, but the slab component decreases more rapidly than the 2D component. The theoretical σ_{c}^* is consistent with the observed σ_{sl}^c , whereas the theoretical σ_{c}^{∞} is larger than the observed $\sigma_{2\mathrm{D}}^c$ below $\sim 100~R_{\odot}$, and thereafter is consistent with observed $\sigma_{2\mathrm{D}}^c$. Observationally, the 2D cross helicity is smaller than the slab cross helicity.

NI MHD turbulence transport theory can be used to study the radial evolution of solar wind density fluctuations as illustrated in Figure 1(G). Both the theoretical and observed density fluctuations decrease as a function of heliocentric distance.

Similar to the turbulence energy, the 2D correlation length $\lambda_{\rm 2D}$ cannot be observed near the perihelion. In Figure 2, red stars and cyan diamonds denote the observed 2D correlation length measured by PSP and SolO, respectively. The slab correlation length λ_{sl} is observed from the perihelion to ~ 176 R_{\odot} as denoted by blue stars and black diamonds. Figure 2(A) shows that the observed correlation length λ_{sl}^+ of the slab energy in outward propagating modes derived from the PSP measurements increases more rapidly than that obtained from the SolO measurements. The observed 2D outward Elsässer energy correlation length $\lambda_{\rm 2D}^+$ measured by PSP does not show a clear radial trend, whereas the $\lambda_{\rm 2D}^+$ derived from SolO measurements increases with distance. The theoretical $\lambda_{\rm sl}^+$ (blue curve) is in reasonable accord with the observed $\lambda_{\rm sl}^+$. The theoretical $\lambda_{\rm sl}^+$ (red curve) agrees reasonably with $\lambda_{\rm 2D}^+$ inferred from SolO measurements, but is lower than derived from PSP

measurements. The radial profile of the theoretical correlation length of the 2D inward Elsässer energy (λ_{∞}^{-}) is shown in Figure 2(B) to be close to that observed, while the theoretical λ_{*}^{-} increases more rapidly than the observed λ_{sl}^{-} .

After the initial drop, the theoretical 2D and slab correlation lengths of the residual energy increase slightly in a similar fashion to that of the corresponding observed correlation lengths (Figure 2(C)). The observed 2D and slab correlation lengths of the residual energy are larger than that of the corresponding theoretical residual energy correlation lengths. Figure 2(D) shows that the theoretical and observed 2D correlation lengths of the magnetic field fluctuations are approximately similar. The theoretical slab correlation length λ_B^* is close to the PSP measurements, but is larger than that derived from SolO measurements. Finally, the theoretical 2D and slab correlation lengths of the velocity fluctuations are consistent with the corresponding observed correlation lengths with increasing heliocentric distance.

6. Radial Evolution of Background Solar Wind Profile

The solar wind model and the NI MHD 2D and slab turbulence transport equations are coupled. Therefore, the background solar wind and turbulence influence each other. Coulomb collisions between the solar wind protons and electrons are included in the solar wind proton and electron pressure equation, but this is not as effective as the turbulent heating term. Due to both the turbulent dissipation term and Coulomb collisions between protons and electrons, the proton temperature decreases more slowly than predicted by adiabatic cooling. In Figure 3(A), the theoretical solar wind proton temperature (black curve) decreases with increasing heliocentric distance. However, the theoretical proton temperature is larger than the observed proton temperature (orange and light

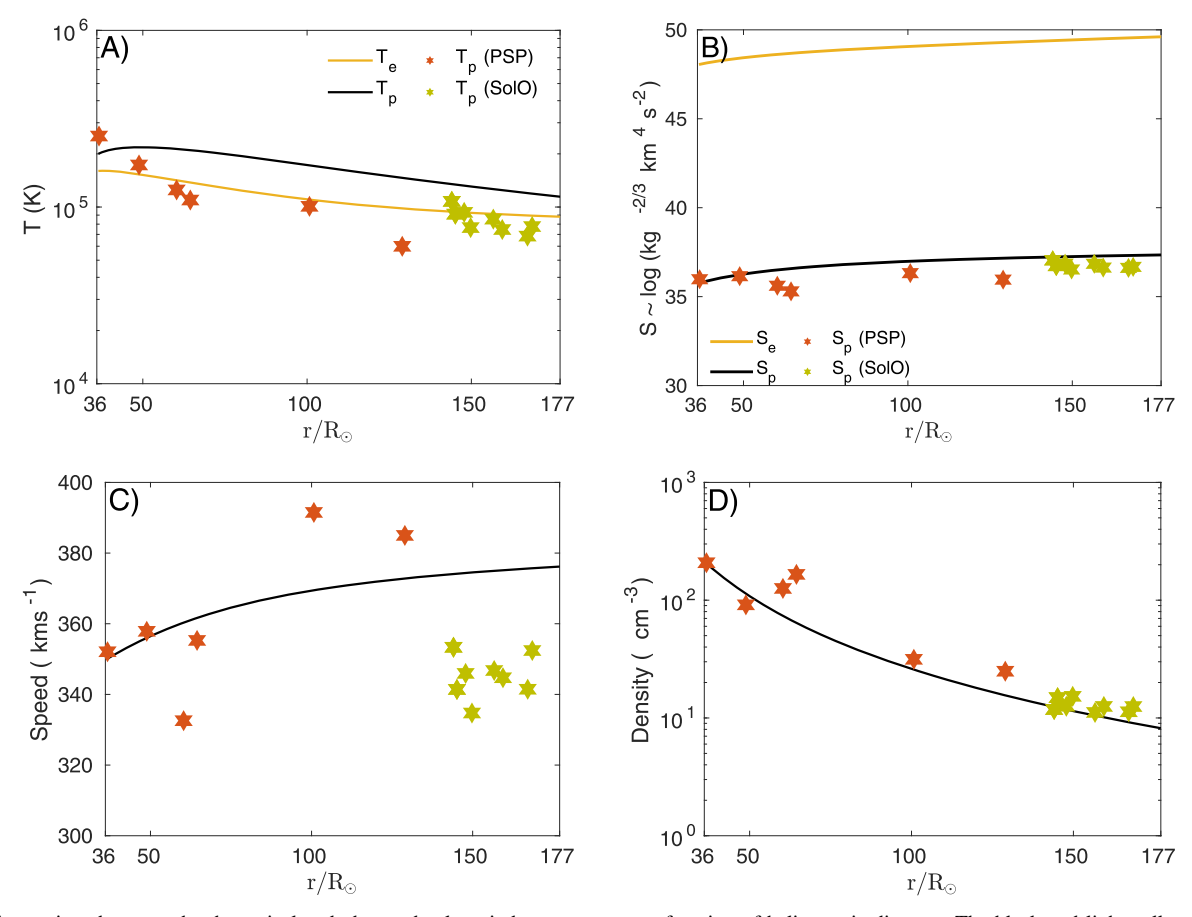


Figure 3. Comparison between the theoretical and observed solar wind parameters as a function of heliocentric distance. The black and light yellow solid curves denote the theoretical solutions. The brown and light green stars denote the observed solar wind parameters corresponding to PSP and SolO measurements, respectively.

green stars). Besides the turbulent dissipation term and Coulomb collisions term, the electron heat flux also influences the radial profile of the electron temperature. In Figure 3(A), the light orange curve shows the theoretical electron temperature, which decreases gradually from 36.66 to $\sim 100 R_{\odot}$, and then decreases more slowly with increasing heliocentric distance due to the electron heat flux. The dissipation of turbulence also leads to an increase in the solar wind proton and electron entropy with increasing heliocentric distance (Adhikari et al. 2020b, 2021b). As shown in Figure 3(B), the theoretical solar wind proton entropy (black curve) increases slightly from about 36.66 to about 177 R_{\odot} in a similar fashion to that of the observed proton entropy of PSP (orange stars) and SolO (light green stars). Similarly, the theoretical electron entropy (light orange curve) also increases gradually with increasing heliocentric distance.

Because the dissipated turbulence energy heats the solar wind protons and electrons, this leads to an increase in the thermal proton and electron pressure gradients. As a result, the solar wind speed increases with distance, as shown by the black curve in Figure 3(C). In the figure, the theoretical solar wind speed (black curve) is close to the observed solar wind speed measured by PSP (orange stars), but is higher than that measured by SolO (light green stars). In Figure 3(D), the theoretical solar wind proton density (black curve) and the observed proton density measured by PSP (orange stars) and SolO (light green stars) decrease with increasing heliocentric distance, and are consistent.

7. Discussion and Conclusions

We used a new data analysis method (M2) to calculate the 2D and slab Elsässer energies, fluctuating magnetic and kinetic energies, normalized residual energy and cross helicity, and the 2D and slab correlation lengths corresponding to Elsässer energies, residual energy, and the fluctuating kinetic and magnetic energies. We also calculated the 2D and slab turbulence energies from the Belcher & Davis (1971) approach (M1). M1 and M2 calculate the transverse and parallel turbulence components relative to the mean magnetic field direction. The parallel turbulence component is regarded as compressible turbulence, and the transverse turbulence component as incompressible turbulence, being either Alfvénic or 2D. M2 first calculates the R, T, and N components of the perpendicular and parallel fluctuating vectors, and then calculates the transverse and parallel variances of the turbulence energies and correlation lengths. Whereas M1 directly calculates the transverse and parallel variances of the turbulence energies. M2 has an advantage over M1 because M2 allows us to calculate the parallel and transverse correlation lengths.

In this work, we calculated the transverse turbulence energy using M1 and M2, and the transverse correlation length using M2 for slow solar wind data sets from the first orbits of PSP and SolO. The slab turbulence component was determined from those transverse turbulence components that are observed in flows satisfying $0^{\circ} < \theta_{\rm UB} < 25^{\circ}$ ($155^{\circ} < \theta_{\rm UB} < 180^{\circ}$). The 2D turbulence component was identified from those transverse turbulence fluctuations that are observed

when $65^{\circ} < \theta_{UB} < 115^{\circ}$, where θ_{UB} is the angle between the mean magnetic and mean flow velocity. Specifically, we used the geometry between the background fields to identify the incompressible 2D and slab components. 2D turbulence can be identified (and measured) in the solar wind when the mean magnetic field and mean solar wind flow vector are orthogonal, whereas slab turbulence can be measured when the two are aligned. This approach is closely related to the Bieber et al. (1996) approach.

We studied the radial evolution of anisotropic MHD turbulence by comparing the theoretical results of the NI MHD turbulencedriven solar wind model with PSP and SolO measurements. We compared the theoretical and observed 2D and slab turbulence energies, and 2D and slab correlation lengths as a function of radial distance. In Adhikari et al. (2021c), we compared the theoretical results of the NI MHD turbulence transport model equations with SolO measurements, in which we incorrectly associated the observed transverse turbulence energy as exclusively the 2D turbulence energy, and the parallel turbulence energy as the slab turbulence energy. In this manuscript, we correctly compared the theoretical results of the NI MHD turbulence transport model equations with the observed 2D and slab turbulence components, where we determined the 2D and slab turbulence components based on θ_{UB} . We summarize our findings as follows.

- The 2D turbulence energies obtained from M1 and M2 are approximately equal and show similar radial trends with increasing heliocentric distance. Similarly, the slab turbulence energies derived from M1 and M2 are similar with distance.
- 2. PSP observed the slab turbulence energy and the slab correlation length near the perihelion of the first orbit, and not the 2D turbulence energy and the 2D correlation length. During its first encounter, PSP observed primarily the slab turbulence component and not the 2D turbulence component over the radial distance 36.66–129 R_{\odot} . Note that the observed results correspond to the energy-containing range scale that is described by the energy-containing range turbulence transport model equations. SolO observed 2D and slab turbulence components frequently over the distance 142–176 R_{\odot} . Although the 2D turbulence component is invisible to PSP near perihelion, the observed 2D and slab fluctuating magnetic energy and energy in backward propagating modes observed by SolO and PSP show that 2D turbulence is the dominant component. For PSP, θ_{UB} corresponding to long intervals is usually small so that only/primarily transverse fluctuations with a parallel wavevector can be measured (assuming the Taylor hypothesis holds). SolO can identify advected 2D transverse fluctuations with wavevectors orthogonal to the mean magnetic field because there are more intervals with $\theta_{\rm UB} \sim 90^{\circ}$. Of course, as we have emphasized repeatedly, transverse 2D fluctuations are almost certainly present in magnetic field-aligned flows but cannot be observed by, e.g., PSP, and vice versa with regard to Alfvénic fluctuations in orthogonal solar wind flows.
- 3. The theoretical and observed 2D and slab outward Elsässer energies decrease with increasing heliocentric distance with theory predicting that the 2D energy density is dominant. PSP measurements do not show clearly whether the 2D or the slab outward Elsässer energy

- dominates, unlike SolO measurements, which reveal a clear dominance of the 2D component.
- 4. PSP and SolO observations show clearly that the 2D inward Elsässer energy exceeds that of the slab, consistent with theory. The same is true for the fluctuating magnetic energy density. SolO confirms the same result for the kinetic energy density, but this is less clear from PSP measurements. All theoretical and observed energy densities (inward Elsässer, magnetic, kinetic) decrease with increasing heliocentric distance.
- 5. Observationally and theoretically, slab turbulence is less magnetically dominated than the 2D turbulence, and both slab and 2D normalized residual energies become more negative with increasing distance.
- 6. The theoretical and observed slab normalized cross helicity is larger than the theoretical and observed 2D normalized cross helicity over the distance ~ 36.66 –177 R_{\odot} , indicating that slab turbulence is Alfvénic. The theoretical and observed 2D and slab normalized cross helicity show good agreement as a function of heliocentric distance.
- 7. The theoretical and observed 2D and slab correlation lengths of the outward Elsässer energy, fluctuating magnetic energy and fluctuating kinetic energy increase with increasing heliocentric distance, and the slab correlation length is larger than the 2D correlation length. Conversely, 2D and slab correlation lengths of the inward Elsässer energy increase with increasing heliocentric distance.
- 8. The theoretical proton temperature decreases gradually with increasing distance, while the theoretical electron temperature flattens beyond $100~R_{\odot}$ due to the electron heat flux.
- The theoretical and observed proton entropy increases as distance increases in a similar fashion. The theoretical electron entropy also increases as a function of heliocentric distance.
- 10. The theoretical solar wind speed increases slightly as a function of heliocentric distance due to the presence of thermal solar wind proton and electron pressure gradients, and is close to PSP measurements, but larger than SolO measurements.
- 11. The theoretical and observed solar wind density decreases as distance increases in a similar fashion.

This study provides evidence of anisotropic MHD turbulence in the slow solar wind in the presence of the large-scale solar magnetic field. PSP has already completed its 10th orbit, and directly interacted with the Sun for the first time during its 8th orbit by crossing the Alfvén critical surface (Kasper et al. 2021; Zank et al. 2022). SolO is also measuring the solar wind in the inner heliosphere, and moving toward the high latitude region. It will be very interesting to extend the study anisotropic MHD turbulence in both sub-Alfvénic and high latitude solar wind regions using PSP and SolO measurements, respectively, using the data analysis methods (M1 and M2) and the NI MHD turbulence transport model.

We acknowledge the partial support of a Parker Solar Probe contract SV4-84017, an NSF EPSCoR RII-Track-1 cooperative agreement OIA-1655280, and NASA awards 80NSSC20K1783 and 80NSSC21K1319. The SWEAP Investigation and this study are supported by the PSP mission under NASA contract NNN06AA01C.

Appendix NI MHD Turbulence Transport Model Equations

Zank et al. (2017) derived the 12 coupled NI MHD turbulence transport model equations describing the majority and a minority turbulence energies (Elsässer energies and residual energy) and the corresponding energy weighted length scales. Here, we write the 12 coupled turbulence transport equations in terms of the Elsässer energies, residual energy, and the corresponding correlation lengths. The 1D steady-state majority 2D turbulence transport model equations can be written as (Zank et al. 2017)

$$U\frac{d\langle z^{\infty\pm2}\rangle}{dr} + \frac{1}{2}(\langle z^{\infty\pm2}\rangle + E_D^{\infty})\left(\frac{dU}{dr} + \frac{2U}{r}\right) = -2\alpha \frac{\langle z^{\infty\pm2}\rangle\langle z^{\infty\mp2}\rangle^{1/2}}{\lambda_{\infty}^{\pm}} + 2C_{\rm sh}^{\pm} \frac{r_0|\Delta U|V_{A0}^2}{r^2},\tag{16}$$

$$U\frac{dE_D^{\infty}}{dr} + \frac{1}{2}(E_D^{\infty} + E_T^{\infty})\left(\frac{dU}{dr} + \frac{2U}{r}\right) = -\alpha E_D^{\infty}\left(\frac{\langle z^{\infty+2}\rangle^{1/2}}{\lambda_{\infty}^{-}} + \frac{\langle z^{\infty-2}\rangle^{1/2}}{\lambda_{\infty}^{+}}\right) + 2C_{\rm sh}^{E_D}\frac{r_0|\Delta U|V_{A0}^2}{r^2},\tag{17}$$

$$U\frac{d\lambda_{\infty}^{\pm}}{dr} + \frac{E_D^{\infty}}{2\langle z^{\infty\pm 2}\rangle} \left(\frac{\lambda_D^{\infty}}{2} - \lambda_{\infty}^{\pm}\right) \left(\frac{dU}{dr} + \frac{2U}{r}\right) = 2\beta \langle z^{\infty\mp 2}\rangle^{1/2} - 2\beta C_{\rm sh}^{\pm} \frac{r_0|\Delta U|V_{A0}^2}{r^2} \frac{\lambda_{\infty}^{\pm}}{\langle z^{\infty\pm 2}\rangle},\tag{18}$$

$$U\frac{d\lambda_D^{\infty}}{dr} + \frac{\langle z^{\infty+2} \rangle}{2E_D^{\infty}} \left(\frac{dU}{dr} + \frac{2U}{r}\right) \left(\lambda_{\infty}^{+} - \frac{\lambda_D^{\infty}}{2}\right) + \frac{\langle z^{\infty-2} \rangle}{2E_D^{\infty}} \left(\frac{dU}{dr} + \frac{2U}{r}\right) \left(\lambda_{\infty}^{-} - \frac{\lambda_D^{\infty}}{2}\right) = \beta \lambda_D^{\infty} \left(\frac{\langle z^{\infty+2} \rangle^{1/2}}{\lambda_{\infty}^{-}}\right)$$

$$+\frac{\langle z^{\infty-2}\rangle^{1/2}}{\lambda_{\infty}^{+}}\right) - 2\beta C_{\rm sh}^{E_D} \frac{r_0 |\Delta U| V_{A0}^2}{r^2} \frac{\lambda_D^{\infty}}{E_D^{\infty}}.$$
 (19)

The first term on the rhs of Equation (16) is the nonlinear dissipation term for the quasi-2D Elsässer energies. In Equation (17), the first term on the rhs defines the decay of the quasi-2D residual energy through the inertial range. The second term in Equations (16) and (17) is the turbulent shear source associated with the interaction of fast and slow streams, and $C_{\rm sh}^{\pm}$ and $C_{\rm sh}^{E_D}$ denote the strengths of the sources. The parameter $|\Delta U|$ denotes the velocity difference between the fast and slow solar wind speed, and $V_{\rm A0}$ is the Alfvén velocity at a reference point r_0 . The parameters $\beta(=\alpha/2)$ and α are the von Kármán–Taylor constants.

We consider the Parker spiral magnetic field in the form given by Weber & Davis (1967)

$$B = B_a \left(\frac{r_a}{r}\right)^2 \left[1 + \left(\frac{\Omega r}{U}\right)^2 \left(1 - \left(\frac{r_a}{r}\right)^2\right)^2 \sin^2\theta\right]^{1/2},\tag{20}$$

where the subscript a represents the reference point r_a . We assume the reference point $r_a \approx 10R_{\odot}$, where R_{\odot} is a solar radius. We use $B_a = 1.08 \times 10^3$ nT.

The 1D steady-state transport equations for NI/slab turbulence can be written as (Zank et al. 2017)

$$(U \mp V_A) \frac{d\langle z^{*\pm 2} \rangle}{dr} + \frac{1}{2} \left(\frac{dU}{dr} + \frac{2U}{r} \right) (\langle z^{*\pm 2} \rangle - E_D^*) + 4b \frac{U \pm V_A}{r} E_D^* \mp \frac{1}{2} (\langle z^{*\pm 2} \rangle - E_D^*) \frac{V_A}{\rho} \frac{d\rho}{dr}$$

$$= -2\alpha \frac{\langle z^{*\pm 2} \rangle \langle z^{\infty \mp 2} \rangle^{1/2}}{\lambda_{\infty}^{\pm}} + 2C_{\text{sh}}^{*\pm} \frac{r_0 |\Delta U| V_{A0}^2}{r^2},$$
(21)

$$U\frac{dE_{D}^{*}}{dr} + \frac{1}{2} \left(\frac{dU}{dr} + \frac{2U}{r} \right) (E_{D}^{*} - E_{T}^{*}) + 4b \frac{U}{r} E_{T}^{*} - 4b \frac{V_{A}}{r} E_{C}^{*} - \frac{V_{A}}{2\rho} \frac{d\rho}{dr} E_{C}^{*} = -\alpha E_{D}^{*} \left(\frac{\langle z^{\infty-2} \rangle^{1/2}}{\lambda_{\infty}^{+}} + \frac{\langle z^{\infty+2} \rangle^{1/2}}{\lambda_{\infty}^{-}} \right) + 2C_{\text{sh}}^{*E_{D}} \frac{r_{0} |\Delta U| V_{A0}^{2}}{r^{2}},$$
(22)

$$(U \mp V_A)\frac{d\lambda_*^{\pm}}{dr} + \frac{E_D^*}{2\langle z^{*\pm 2}\rangle} \left(\lambda_*^{\pm} - \frac{\lambda_D^*}{2}\right) \left(\frac{dU}{dr} + \frac{2U}{r}\right) - 4b\frac{U \pm V_A}{r} \frac{E_D^*}{\langle z^{*\pm 2}\rangle} \left(\lambda_*^{\pm} - \frac{\lambda_D^*}{2}\right)$$

$$\mp \frac{V_A}{2\rho} \frac{d\rho}{dr} \frac{E_D^*}{\langle z^{*\pm 2} \rangle} \left(\lambda_*^{\pm} - \frac{\lambda_D^*}{2} \right) = 2\beta \frac{\lambda_*^{\pm}}{\lambda_{\infty}^{\pm}} \langle z^{\infty \mp 2} \rangle^{1/2} - 2\beta C_{\rm sh}^{*\pm} \frac{r_0 |\Delta U| V_{A0}^2}{r^2} \frac{\lambda_*^{\pm}}{\langle z^{*\pm 2} \rangle}, \tag{23}$$

$$U\frac{d\lambda_D^*}{dr} + \left[\frac{\langle z^{*+2}\rangle}{2E_D^*} \left(\frac{\lambda_D^*}{2} - \lambda_*^+\right) + \frac{\langle z^{*-2}\rangle}{2E_D^*} \left(\frac{\lambda_D^*}{2} - \lambda_*^-\right)\right] \left(\frac{dU}{dr} + \frac{2U}{r}\right) - 4b\frac{U}{r}\frac{E_T^*}{E_D^*}\lambda_D^*$$

$$+4b\frac{V_{A}}{r}\frac{E_{C}^{*}}{E_{D}^{*}}\lambda_{D}^{*}+\frac{V_{A}}{2\rho}\frac{d\rho}{dr}\frac{E_{C}^{*}}{E_{D}^{*}}\lambda_{D}^{*}+4b\frac{U}{r}\frac{\langle z^{*+2}\rangle\lambda_{+}^{+}+\langle z^{*-2}\rangle\lambda_{-}^{-}}{E_{D}^{*}}-4b\frac{V_{A}}{r}\frac{\langle z^{*+2}\rangle\lambda_{+}^{+}-\langle z^{*-2}\rangle\lambda_{-}^{-}}{E_{D}^{*}}$$

$$-\frac{V_A}{2\rho} \frac{d\rho}{dr} \frac{\langle z^{*+2} \rangle \lambda_*^+ - \langle z^{*-2} \rangle \lambda_*^-}{E_D^*} = \beta \lambda_D^* \left(\frac{\langle z^{\infty-2} \rangle^{1/2}}{\lambda_\infty^+} + \frac{\langle z^{\infty+2} \rangle^{1/2}}{\lambda_\infty^-} \right) - 2\beta C_{\text{sh}}^{*E_D} \frac{r_0 |\Delta U| V_{A0}^2}{r^2} \frac{\lambda_D^*}{E_D^*}, \tag{24}$$

where V_A is the Alfvén velocity. The parameter b describes the geometry of NI/slab turbulence and is related to the closure assumption for the off-diagonal two-point correlations. In Equation (21), the first term on the rhs is the nonlinear dissipation term for the NI/slab energy in forward and backward propagating modes. On the rhs of Equation (22), the first term defines the decay of the NI/slab residual energy. The second term on the rhs of Equations (21) and (22) is the shear source of turbulence for the NI/slab energy in forward/backward propagating modes, and the residual energy with strengths $C_{\rm sh}^{*\pm}$ and $C_{\rm sh}^{*E_D}$, respectively.

The 1D steady-state transport equation for the variance of the density fluctuations can be written as (Zank et al. 2017, 2018; Adhikari et al. 2017a)

$$U\frac{d\langle\rho^{\infty2}\rangle}{dr} + 2\langle\rho^{\infty2}\rangle\frac{dU}{dr} + 4\frac{U}{r}\langle\rho^{\infty2}\rangle = -\alpha\frac{\langle u^{\infty2}\rangle^{1/2}\langle\rho^{\infty2}\rangle}{l_u^{\infty}} + \eta_1\langle\rho^{\infty2}\rangle_0\frac{r_0^2|\Delta U|}{r^3}.$$
 (25)

The second term on the rhs of Equation (25) is the turbulent shear source for the density variance with strength η^1 , and $\langle \rho^{\infty 2} \rangle_0$ is the density variance at a reference position r_0 .

ORCID iDs

L. Adhikari https://orcid.org/0000-0003-1549-5256 G. P. Zank https://orcid.org/0000-0002-4642-6192 L.-L. Zhao https://orcid.org/0000-0002-4299-0490 D. Telloni https://orcid.org/0000-0002-6710-8142

References

```
Adhikari, L., Zank, G. P., Bruno, R., et al. 2015, ApJ, 805, 63
Adhikari, L., Zank, G. P., Hu, Q., & Dosch, A. 2014, ApJ, 793, 52
Adhikari, L., Zank, G. P., Hunana, P., et al. 2017a, ApJ, 841, 85
Adhikari, L., Zank, G. P., Telloni, D., et al. 2017b, ApJ, 851, 117
Adhikari, L., Zank, G. P., Zhao, L. L., et al. 2018, JPhCS, 1100, 012001
Adhikari, L., Zank, G. P., Zhao, L. L., et al. 2020a, ApJS, 246, 38
Adhikari, L., Zank, G. P., & Zhao, L. L. 2021a, Fluids, 6, 368
Adhikari, L., Zank, G. P., Zhao, L. L., et al. 2021c, A&A, 656, A6
Adhikari, L., Zank, G. P., Zhao, L. L., Nakanotani, M., & Tasnim, S. 2021b,
   A&A, 650, A16
Adhikari, L., Zank, G. P., Zhao, L. L., & Webb, G. M. 2020b, ApJ,
  891, 34
Bale, S. D., Goetz, K., Harvey, P. R., et al. 2016, SSRv, 204, 49
Bandyopadhyay, R., & McComas, D. J. 2021, ApJ, 923, 193
Barakat, A. R., & Schunk, R. W. 1982, PIPh, 24, 389
Belcher, J. W., & Davis, L., Jr 1971, JGR, 76, 3534
Bieber, J. W., Wanner, W., & Matthaeus, W. H. 1996, JGR, 101, 2511
Breech, B., Matthaeus, W. H., Cranmer, S. R., Kasper, J. C., & Oughton, S.
  2009, JGRA, 114, A09103
Breech, B., Matthaeus, W. H., Minnie, J., et al. 2008, JGRA, 113, 8105
Bruno, R., Bavassano, B., Pietropaolo, E., Carbone, V., & Veltri, P. 1999, GeoRL,
  26, 3185
Bruno, R., & Telloni, D. 2015, ApJL, 811, L17
Chhiber, R., Usmanov, A. V., Matthaeus, W. H., Parashar, T. N., &
   Goldstein, M. L. 2019, ApJS, 242, 12
Coleman, P. J., Jr 1968, ApJ, 153, 371
Cranmer, S. R., Matthaeus, W. H., Breech, B. A., & Kasper, J. C. 2009, ApJ,
Dasso, S., Matthaeus, W. H., Weygand, J. M., et al. 2008, Proc. of the 30th Int.
   Cosmic Ray Conf. (Mexico City, Mexico) ed. R. Caballero et al., 625
Dasso, S., Milano, L. J., Matthaeus, W. H., & Smith, C. W. 2005, ApJL,
  635, L181
Dosch, A., Adhikari, L., & Zank, G. P. 2013, in 13th Int. Solar Wind Conf., AIP
   Conf. Ser. 1539, ed. G. P. Zank et al. (Melville, NY: AIP), 155
Engelbrecht, N. E., & Strauss, R. D. T. 2018, ApJ, 856, 159
Ghosh, S., Matthaeus, W. H., Roberts, D. A., & Goldstein, M. L. 1998, JGR,
   103, 23705
Goldreich, P., & Sridhar, S. 1995, ApJ, 438, 763
Grappin, R. 1986, PhFl, 29, 2433
Grappin, R., Velli, M., & Mangeney, A. 1993, PhRvL, 70, 2190
Hamilton, K., Smith, C. W., Vasquez, B. J., & Leamon, R. J. 2008, JGRA, 113,
He, J., Tu, C., Marsch, E., Bourouaine, S., & Pei, Z. 2013, ApJ,
   773, 72
Horbury, T. S., Balogh, A., Forsyth, R. J., & Smith, E. J. 1995, GeoRL,
```

Horbury, T. S., Forman, M., & Oughton, S. 2008, PhRvL, 101, 175005

```
Horbury, T. S., O'Brien, H., Carrasco Blazquez, I., et al. 2020, A&A, 642, A9
Horbury, T. S., Wicks, R. T., & Chen, C. H. K. 2012, SSRv, 172, 325
Kasper, J. C., Abiad, R., Austin, G., et al. 2016, SSRv, 204, 131
Kasper, J. C., Klein, K. G., Lichko, E., et al. 2021, PhRvL,
   127, 25501
Leamon, R. J., Smith, C. W., Ness, N. F., Matthaeus, W. H., & Wong, H. K.
   1998, JGR, 103, 4775
MacBride, B. T., Smith, C. W., & Vasquez, B. J. 2010, JGRA, 115, A07105
Marsch, E., & Tu, C. Y. 1993, JGR, 98, 21045
Matthaeus, W. H., Dasso, S., Weygand, J. M., et al. 2005, PhRvL,
   95, 231101
Matthaeus, W. H., Ghosh, S., Oughton, S., & Roberts, D. A. 1996, JGR,
   101, 7619
Matthaeus, W. H., Goldstein, M. L., & Roberts, D. A. 1990, JGR,
   95, 20673
Matthaeus, W. H., Zank, G. P., Smith, C. W., & Oughton, S. 1999, PhRvL,
Milano, L. J., Dasso, S., Matthaeus, W. H., & Smith, C. W. 2004, PhRvL, 93,
Montgomery, D. 1982, PhyS, 1982, 83
Montgomery, D., & Turner, L. 1981, PhFl, 24, 825
Narita, Y., Glassmeier, K.-H., Sahraoui, F., & Goldstein, M. L. 2010, PhRvL,
   104, 171101
Osman, K. T., & Horbury, T. S. 2007, ApJL, 654, L103
Osman, K. T., & Horbury, T. S. 2009a, AnGeo, 27, 3019
Osman, K. T., & Horbury, T. S. 2009b, JGRA, 114, A06103
Oughton, S., Matthaeus, W. H., Wan, M., & Osman, K. T. 2015, RSPTA, 373,
   20140152
Owen, C. J., Bruno, R., Livi, S., et al. 2020, A&A, 642, A16
Pilipp, W. G., Muehlhaeuser, K. H., Miggenrieder, H., Rosenbauer, H., &
   Schwenn, R. 1990, JGR, 95, 6305
Pine, Z. B., Smith, C. W., Hollick, S. J., et al. 2020, ApJ, 900, 93
Podesta, J. J. 2009, ApJ, 698, 986
Ruiz, M. E., Dasso, S., Matthaeus, W. H., Marsch, E., & Weygand, J. M. 2011,
   JGRA, 116, A10102
Shebalin, J. V., Matthaeus, W. H., & Montgomery, D. 1983, JPIPh,
Shiota, D., Zank, G. P., Adhikari, L., et al. 2017, ApJ, 837, 75
Smith, C. W., Vasquez, B. J., & Hamilton, K. 2006, JGRA, 111, 9111
Telloni, D., Carbone, F., Bruno, R., et al. 2019, ApJ, 887, 160
Wang, X., Tu, C., & He, J. 2014, ApJL, 783, L9
Wang, X., Tu, C., He, J., et al. 2015, ApJL, 810, L21
Wang, X., Tu, C., & He, J. 2019, ApJ, 871, 93
Weber, E. J., & Davis, L., Jr 1967, ApJ, 148, 217
Weygand, J. M., Matthaeus, W. H., Dasso, S., et al. 2009, JGRA,
   114, A07213
Weygand, J. M., Matthaeus, W. H., Dasso, S., & Kivelson, M. G. 2011, JGRA,
   116, A08102
Weygand, J. M., Matthaeus, W. H., Kivelson, M. G., & Dasso, S. 2013, JGRA,
   118, 3995
Wicks, R. T., Horbury, T. S., Chen, C. H. K., & Schekochihin, A. A. 2010,
Zank, G. P. 2014, in Transport Processes in Space Physics and Astrophysics, ed.
   G. P. Zank et al., Vol. 877 (Berlin: Springer)
Zank, G. P., Adhikari, L., Hunana, P., et al. 2017, ApJ, 835, 147
Zank, G. P., Adhikari, L., Zhao, L. L., et al. 2018, ApJ, 869, 23
```

Zank, G. P., Dosch, A., Hunana, P., et al. 2012, ApJ, 745, 35

```
Zank, G. P., & Matthaeus, W. H. 1992a, JPIPh, 48, 85
Zank, G. P., & Matthaeus, W. H. 1992b, JGR, 97, 17189
Zank, G. P., & Matthaeus, W. H. 1993, PhFl, 5, 257
Zank, G. P., Matthaeus, W. H., & Smith, C. W. 1996, JGR, 101, 17093
Zank, G. P., Nakanotani, M., Zhao, L. L., Adhikari, L., & Telloni, D. 2020, ApJ, 900, 115
Zank, G. P., Zhao, L. L., Adhikari, L., et al. 2021, PhPl, 28, 080501
```

```
Zank, G. P., Zhao, L. L., Adhikari, L., et al. 2022, ApJL, 926, L16
Zhao, L.-L., Adhikari, L., Zank, G. P., Hu, Q., & Feng, X. S. 2018, ApJ, 856, 94
Zhao, L. L., Zank, G. P., Adhikari, L., et al. 2020, ApJ, 898, 113
Zhao, L. L., Zank, G. P., Adhikari, L., & Nakanotani, M. 2022, ApJL, 924, L5
Zhou, Y., & Matthaeus, W. H. 1990, JGR, 95, 10291
```